Gyrokinetic turbulence simulations at high plasma beta

M.J. Pueschel, M. Kammerer, and F. Jenko

Max-Planck-Institut für Plasmaphysik,

EURATOM Association, D-85748 Garching, Germany

Abstract

Electromagnetic gyrokinetic turbulence simulations employing Cyclone Base Case parameters are presented for β values up to and beyond the kinetic ballooning threshold. The β scaling of the turbulent transport is found to be linked to a complex interplay of linear and nonlinear effects. Linear investigation of the kinetic ballooning mode is performed in detail, while nonlinearly, it is found to dominate the turbulence only in a fairly narrow range of β values just below the respective ideal limit. The magnetic transport scales like β^2 and is well described by a Rechester-Rosenbluth-type ansatz.

1

I.   INTRODUCTION

The normalized plasma pressure β is one of the most essential dimensionless parameters characterizing a fusion plasma. Since it governs both the reaction rates ($\propto \beta^2$) and the bootstrap fraction ($\propto \beta$), a large β value is highly desirable for future power plants. While large-scale – magnetohydrodynamic (MHD) – instabilities of various types are known to impose an upper β limit, small-scale – gyrokinetic – instabilities driving turbulent fluctuations may also affect the plasma performance in the high β regime. This may happen in basically two ways. First, various electrostatic microinstabilities like ion temperature gradient (ITG) modes or trapped electron modes (TEMs) along with the respective kinds of turbulence are altered in the presence of magnetic field fluctuations. The anomalous transport properties may thus be changed significantly with respect to the low β limit, potentially affecting the plasma confinement. Second, in the framework of a gyrokinetic description, kinetic ballooning modes (KBMs) may be destabilized below the MHD ballooning limit, causing very large transport levels and effectively reducing the achievable plasma β. Consequently, it is important to know exactly where the kinetic limit lies, and also how the transport behaves close to that operational point.

Tokamak experiments have yielded widely differing results for the scaling of the energy confinement time with β. While for some, very little or no dependence was reported [1, 2], a strong degradation of the confinement with increasing β was found for others [3, 4]. One possible explanation is that different experiments are operated in different instability regimes with different β scalings, thus causing these apparently inconsistent results – but edge effects may also play an important role. This clearly shows that it is highly desirable to gain a more solid understanding of the underlying physical processes. While previous theoretical research for core parameters, based on (gyro-)fluid (neglecting trapped electron effects) [5–7] or gyrokinetic [8–11] simulations, consistently finds a significant decline of ITG-induced transport with increasing β (holding all other dimensionless simulation parameters fixed), the behavior of turbulent transport at high β remains poorly understood. Many important questions are still unanswered. Among these are: What kind of transport levels should one expect? Will there be regime transitions, e.g., from ITG to TEM turbulence, and if so, what is their nature? What is the role of magnetic transport as one approaches the MHD ballooning limit? By how much can the KBM threshold go below the respective MHD value,

2

and how does the turbulence react to the presence of weakly unstable KBMs? It is the main goal of the present paper to address these questions by means of gyrokinetic simulations with the GENE [12, 13] code, using the so-called Cyclone Base Case [14] parameters.

The remainder of this work is structured in the following way. In Section II, we study linear properties of ITG modes and TEMs as a function of β, leading to some expectations concerning the resulting nonlinear behavior. This is followed by an in-depth discussion of the KBM threshold in Section III, employing the possibility to use GENE as a linear eigenvalue solver, providing access also to subdominant unstable modes. In this context, the dependence of the critical KBM β on plasma parameters will be investigated. From this linear basis, we then move on to nonlinear results in Section IV. Turbulence transport levels all the way from the electrostatic limit well into the KBM regime are reported, confirming and extending previous work. We will discuss the nature of regime transitions including, in particular, the value of the nonlinear threshold for KBMs. Moreover, there will be a focus on the resulting level of magnetic transport. In Section V, we will then try to understand these nonlinear results with the help of further simulation diagnostics and two transport models. Finally, some conclusions are given in Section VI.

II. GYROKINETIC SIMULATIONS: BACKGROUND AND LINEAR β DEPENDENCE

A. Simulation details

The present work aims at studying – by means of linear and nonlinear gyrokinetic simulations – the behavior of tokamak core turbulence for β ranging from zero (electrostatic limit) to values larger than the kinetic ballooning threshold. From the various possible definitions for β, we choose

$$\beta \equiv \beta_{\mathrm{e}} \equiv \frac{8\pi n_{\mathrm{e0}} T_{\mathrm{ref}}}{B_{\mathrm{ref}}^2} \ , \tag{1}$$

with n_{e0} being the equilibrium electron density, T_{ref} the reference temperature, and B_{ref} the reference magnetic field.

The following numerical investigations are performed employing the GENE [12, 13] code which solves the nonlinear gyrokinetic equations [15] (in the local limit) for an arbitrary number of (active or passive) particle species on a fixed grid in five-dimensional phase space.

3

It includes electromagnetic effects as well as collisions (involving pitch angle and energy scattering [16]) and real tokamak geometry (via an interface to MHD equilibrium codes [17]). For the purposes of the present work, the latter effects shall be neglected, however, focussing on collisionless situations and employing a simple $\hat{s}$-α model geometry with $\alpha = 0$. For linear computations, GENE can also be run as an eigenvalue solver, providing access to subdominant unstable modes [18]. This feature will prove useful, in particular, in the context of determining the linear KBM threshold.

In terms of physical parameters, we will work with the well-known Cyclone Base Case parameters which have also been used in various previous publications (see, e.g., Refs. [10, 11]). This choice allows for easier code-code comparisons and may be expected to represent rather typical core turbulence conditions. The respective parameter set reads: $\omega_{\mathrm{Ti}} \equiv R/L_{\mathrm{Ti}} = 6.89 = R/L_{\mathrm{Te}} \equiv \omega_{\mathrm{Te}}$, $\omega_{\mathrm{n}} \equiv R/L_{\mathrm{n}} = 2.22$, $T_{\mathrm{ref}} = T_{\mathrm{i}} = T_{\mathrm{e}}$, $\hat{s} = 0.786$, $q = 1.4$, and $\epsilon_t \equiv r/R = 0.18$. Here, R is the major radius, L_{Ti}, L_{Te}, and L_{n} are the characteristic gradient lengths, T_{i} and T_{e} are the ion and electron temperature, respectively, $\hat{s}$ is the magnetic shear, q is the safety factor, and r is the relevant minor radius.

Let us now turn to the simulation parameters. We will use kinetic electrons with a mass of $m_{\mathrm{e}}/m_{\mathrm{i}} = 5.669 \times 10^{-4}$, corresponding to a hydrogen plasma. The simulation box is defined as follows. For linear runs, we take $L_y = 2\pi/k_y$ and $L_x = 1/(k_y \hat{s})$, while for nonlinear runs, we choose $L_y = 125.66$ and $L_x = 101.78$. In addition, we always have $L_z = 2\pi q R$, where x is the radial, y is the binormal, and z is the parallel coordinate. The perpendicular coordinates are normalized with respect to the ion gyroradius ρ_{i}, and consequently, wave numbers are given in units of ρ_{i}^{-1}. Concerning velocity space coordinates, we use the parallel velocity $v_\parallel$, which is given in units of $(2T_j/m_j)^{1/2}$ for species $j = \mathrm{i}, \mathrm{e}$, and the magnetic moment $\mu = mv_\perp^2/(2B)$ which is normalized accordingly. Throughout this paper, we take $L_{v_\parallel} = v_{\parallel,\mathrm{max}} = 3$ and $L_\mu = \mu_{\mathrm{max}} = 9$. The grid resolution is described below.

B. Linear β scan

To get an idea what kind of microinstabilities are likely to be responsible for driving the turbulence for our nominal parameters in various β regimes, we first perform some linear gyrokinetic simulations. Here, we focus on $k_y = 0.2$ which corresponds roughly to the position of the maximum of the nonlinear transport spectrum, as we will see later.

4

Convergence studies in every instability regime lead us to use the following set of grid parameters which guarantee good convergence across the entire β range: $N_x = 24$ (12 modes per sign), $N_z = 24$, $N_{v_\parallel} = 96$ (required for the TEMs), and $N_\mu = 16$.

Fig. 1 shows the behavior of the linear growth rate and the frequency as β is varied. For comparison, we have repeated these linear runs with the GS2 [19] code, demonstrating very good agreement and thus the reliability of the displayed data. We find that at low β values, the dominant microinstability is an ITG mode, as expected. With increasing β, the growth rate of this mode is diminished, however, until a TEM takes over. As eigenvalue calculations with GENE show, the latter mode is unstable across the entire β range, and its linear growth rate is practically not influenced by changes in β – in contrast to the ITG mode. It shall be pointed out for future reference that the TEM growth rate is roughly half that of the ITG mode in the electrostatic limit. As is apparent in Fig. 1, at still higher β values, a KBM starts to dominate. Its linear growth rate increases quite rapidly once the respective β threshold is crossed. The real frequency exhibits a positive sign, which, in our convention, corresponds to a drift in the ion diamagnetic direction; moreover, the amplitude of this frequency clearly exceeds the ITG frequency, an effect which is discussed, e.g., in Ref. [20]. Within any one regime, only small modifications of the frequencies are observed. Linearly, one thus has two critical β values (at $k_y = 0.2$): at $\beta = 0.95\%$, a transition from ITG modes to TEMs takes place, and at $\beta = 1.27\%$, KBMs become dominant. We will devote the entire next section to the properties of this latter critical value and its deviation from the MHD prediction.

III. LINEAR KBM THRESHOLDS

It is well known that MHD ballooning modes only become linearly unstable when β exceeds a certain (plasma parameter dependent) threshold. The same is true for their gyrokinetic counterpart, the KBMs. These thresholds need not coincide, however. As has been discussed in various previous publications (see, e.g., Refs. [21–24] for the local case; for radially nonlocal investigations, see, e.g., Ref. [25]), the KBM onset can go significantly below the respective MHD value under certain conditions. Actually, reductions by up to about 50% have been reported in Refs. [23, 24], a claim that was disputed later [26]. At present, it is not clear if those numbers can be confirmed in the context of a reasonably

comprehensive gyrokinetic approach. The linear GENE simulations which will be presented in this section are supposed to shed some light on this very issue.

Since the KBM onset in a $\gamma(\beta)$ plot of the dominant modes is often obscured by other microinstabilities like ITG modes or TEMs (see, e.g., Fig. 1), it is useful to use GENE in its eigenvalue solver mode [18]. Thus, an arbitrary number of coexisting linear modes (both unstable and stable) can be detected. The (subdominant) behavior of the KBMs calculated this way for our nominal physical parameters is shown in Fig. 2. Obviously, the respective linear growth rate crosses into the negative range at $\beta_{\mathrm{crit}} = 1.14\%$. Two things are noteworthy about this finding. Firstly, these particular KBMs (at $k_y = 0.2$) are subject to substantial linear damping below the β threshold, rendering it unlikely that they play a role in respective nonlinear simulations. Secondly, the inferred value for β_{crit} is about 14% below the MHD ballooning limit, which can be estimated to be $\beta_{\mathrm{crit,MHD}} = 0.6\hat{s}/[q_0^2(2\omega_{\mathrm{n}} + \omega_{\mathrm{Ti}} + \omega_{\mathrm{Te}})] = 1.32\%$.

This qualitative behavior is by no means universal, however. For other sets of physical parameters, one can find different scenarios. For example, the KBM can also become marginally stable below the threshold. Such a case, using the nominal physical parameters except for $\omega_{\mathrm{n}} = 3$, $\omega_{\mathrm{Ti}} = 4$, and $\omega_{\mathrm{Te}} = 6$, can be seen in Fig. 3. While an interesting effect in itself, it is more than doubtful, however, that such marginally stable modes can play a significant role in nonlinear simulations. At least for the present case (as will be shown below), KBMs do not become nonlinearly dominant as long as $\gamma_{\mathrm{TEM}} > \gamma_{\mathrm{KBM}}$.

Depending on the physical parameters, the picture can change even more drastically. In Fig. 4, an example (with $\epsilon_t = 0.16$ and $\omega_{\mathrm{n}} = 6$) is shown for which the KBM is continually transformed into a TEM-like instability. While one may use various methods to determine a critical β value (e.g., by taking the value where $\omega = 0$), it is obvious that a precise definition of the KBM threshold is not possible in this case. Similarly, KBM-ITG transformations occur for yet different parameters. For a more in-depth discussion of these transformations, occurring in the neighborhood of so-called exceptional points, see Ref. [18].

Determining the KBM stability threshold by following the mode through the subdominant range until arriving at negative growth rates requires significantly more computational effort than finding the growth rates of dominant modes. If one aims to extract the KBM thresholds for many different sets of physical parameters, this method might thus be somewhat cumbersome. Therefore, we shall show how to arrive at a good estimate for β_{crit} by

looking at more accessible data.

The growth rates for the TEM and KBM regime can be fitted well by linear and quadratic functions, respectively. By taking the intersection of these fit functions, the value $\beta_{\text{crit}}^{\text{dom}}$ can be determined at which γ_{KBM} becomes larger than γ_{TEM}; analogously, $\beta_{\text{crit}}^{\text{extrapol}}$ is defined as the value at which the KBM fit function becomes zero. One thus obtains $\beta_{\text{crit}}^{\text{dom}} = 1.26\%$ and $\beta_{\text{crit}}^{\text{extrapol}} = 1.21\%$ for $k_y = 0.2$. The corresponding results for other values of k_y are shown in Fig. 5. Note that for both the dominant and the extrapolated critical β, the respective minimum lies at $k_y = 0.2$.

At this point, it is worthwhile to make a brief remark concerning the effect of setting α_{MHD} to zero. While this was done in the simulations presented here for comparability purposes, one can easily use values consistent with the respective β. The resulting critical β values for $k_y = 0.2$ are $\beta_{\text{crit}}^{\text{dom}} = 1.26\%$ and $\beta_{\text{crit}}^{\text{extrap}} = 1.22\%$, in excellent agreement with the respective $\alpha_{\text{MHD}} = 0$ results.

One additional aspect of interest is how the KBM threshold depends on the density and temperature gradients. We thus scan each gradient over a range, keeping the respective other gradients fixed to their standard values. Since $\beta_{\text{crit}}^{\text{MHD}}$ is a function of these gradients, it is instructive to look at α_{crit}, as well, for which MHD predicts a constant value. The results of this investigation are shown in Fig. 6. Note that here, only values for $k_y = 0.2$ are included. Obviously, most values of $\alpha_{\text{crit}}^{\text{extrap}}$ deviate only mildly from $\alpha_{\text{crit}}^{\text{MHD}} = 0.472$, especially as far as changes in ω_{Te} and ω_{n} are concerned. However, for large values of ω_{Ti}, α_{crit} is up to about 15% lower than $\alpha_{\text{crit}}^{\text{MHD}}$. This leads to the conclusion that while, in principle, *all* profile gradients play a role in determining the kinetic value of β_{crit}, the biggest effect comes from the ion temperature gradient, which is in line with previous studies [22, 23]. As expected, in almost all cases, $\alpha_{\text{crit}}^{\text{extrap}}$ lies below $\alpha_{\text{crit}}^{\text{MHD}}$; however, as ω_{Ti} is decreased, the KBM stability threshold eventually extends beyond the MHD prediction. While in this regime, no marginally stable low-β behavior was found for $k_y = 0.2$ (as one might have expected taking into consideration the similarly low ω_{Ti} that was used in Fig. 3), the $k_y = 0.1$ counterpart shows indeed such a marginally stable tail. In this case, $\beta_{\text{crit}} = 1.87\%$ (corresponding to $\alpha_{\text{crit}} = 0.526$) which is again closer to the MHD value. This is consistent with the requirement that as $k_y \to 0$, $\beta_{\text{crit}} \to \beta_{\text{crit}}^{\text{MHD}}$.

In summary, one finds that – at least for physical parameters which are relatively close to the Cyclone Base Case set – the reduction of the linear KBM threshold relative to its

MHD counterpart tends to remain below about 20%. Generally, the disappearance of the KBM can occur in (at least) three different ways: it can turn into a damped mode; it can become marginally stable; or it can transition directly into a different mode (like a TEM or an ITG mode). While these investigations help confine the region of influence of KBMs, they merely represent estimates. In order to assess the role of KBMs in fully turbulent systems, nonlinear simulations are called for. This will be the topic of the next section.

IV. TURBULENCE SIMULATIONS: REGIMES AND NONLINEAR KBM ONSET

A. Simulation details and code-code comparison

The most important difference between linear and nonlinear resolution requirements is caused by the magnetic field line flutter. The electrons are prone to react violently to perpendicular disturbances in the magnetic field, and therefore a high parallel resolution is required for somewhat higher β. In consequence, all nonlinear simulations at $\beta \geq 0.7\%$ are done with $N_z = 48$. The perpendicular grid is $N_x = 192$ (positive and negative modes each 96) and $N_{k_y} = 24$. Convergence was tested in the ITG dominant regime at $\beta = 0.8\%$.

An important exercise in numerical simulations is testing the agreement of different codes. Fig. 7 shows that the transport levels obtained with GENE in the ITG regime agree well both qualitatively and quantitatively with results from GYRO reported in Ref. [11]. However, it remains to be seen whether the difference in the linear critical $\beta_{\mathrm{crit}}^{\mathrm{dom}}$ between these codes carries over to nonlinear simulations. In Ref. [10], the decrease of the ion transport with increasing β is smaller, but the transport levels are similar. These comparisons lend reliability to the present simulations. We shall use them as a basis to now explore the high-β regime.

B. Turbulence regimes and nonlinear KBM onset

The nonlinear transport levels over an extended β range are shown in Fig. 8. One finds first a pronounced decrease, followed by a flat region, and then a sudden and steep increase. As becomes apparent, even from this plot, there exist at least two distinct turbulence regimes

8

(dominated, respectively, by ITG modes or TEMs, and KBMs), separated by a transitional point at about $\beta = 1.26\%$. Additionally, one finds qualitative changes at $\beta = 0.8\%$ and $\beta = 1.1\%$. The critical KBM value is actually very close to the linearly determined value (for $k_y = 0.2$) at which the KBM growth rate starts to exceed that of the TEM.

Interpreting the other two thresholds represents a greater difficulty. Looking at phase shifts (see Fig. 9) and changes in the transport spectra (see Fig. 10), one might be led to believe that the nonlinear behavior follows the linear one, including an ITG-TEM transition at roughly the same β. While this picture is supported by a phase-based frequency analysis that includes all radial connections of the extended ballooning structure (without weighing by amplitude), using Fourier transforms (including only the first radial connections) to determine the nonlinear frequencies yields different results. As can be seen in Fig. 11, no negative frequencies occur over the entire β range. Additionally, there is a frequency shift at $\beta = 0.8\%$, and another at $\beta = 1.2\%$. The second value corresponds to the linear onset of KBMs which dominate the frequency signature while not dominating the transport for $\beta \leq \beta_{\text{crit}}^{\text{dom}}$. The intermediate range at $\omega \approx 1.5$ cannot be motivated by the linear physics, however; also, ion electrostatic heat transport exceeds its electron counterpart throughout the range corresponding to TEMs linearly, whereas looking at the ratio of the ion and electron transport in linear simulations, one would expect a much higher electron contribution. This intermediate range might be due to nonlinear interaction of the ITG modes with the TEMs; and possibly, magnetic flutter contributes to the change, as well. Consequently, we label the regime at smaller and moderate β an ITG-TEM regime. Note that for $\beta < 0.8\%$, one finds pure ITG turbulence.

In this context, it should be noted that for a few β values in this scan, the simulations are quite challenging numerically. While *all* simulations find saturation, the ones for $\beta = 1.0\%$ and 1.1% (in the ITG-TEM coexistence regime) and for $\beta = 1.3\%$ and 1.325% (in the KBM regime) display – for the numerical parameters used here – what appears to be a numerical instability in the long-time limit. In these cases, the transport levels would first saturate, and then take off to much larger values after roughly $(200 - 300)R/c_s$. On the other hand, β values between those regions seem not to be affected. E.g., the $\beta = 1.25\%$ simulation shows no sign of a numerical instability during its full duration of $> 500R/c_s$. These difficulties might be related, respectively, to the nonlinear interplay of ITG modes and TEMs (see the discussion below) and to the linear low-k_y behavior of KBMs, but a more detailed analysis

(which turns out to be quite involved and is done in collaboration with other groups) is underway and will be published elsewhere.

Interestingly, the β value for which the turbulence acquires a clear KBM character is very close to the linear quantity $\beta_{\mathrm{crit}}^{\mathrm{dom}}$ (taking its minimum at $k_y = 0.2$) that describes the point at which the KBM growth rate exceeds that of the TEM. In other words, while KBMs already contribute within part of the ITG-TEM regime (where they are already linearly unstable), they only become dominant once the linear KBM dominance threshold is crossed. This means, in turn, that the exact onset point for linear KBMs seems to be of limited practical relevance if other modes are clearly dominant there. Although deviations from this rule of thumb can be envisioned, one is led to think that KBMs are likely to dominate nonlinearly wherever they dominate linearly (in the low-k_y part of the spectrum where the transport usually peaks) and vice versa. This finding further narrows the window of KBM activity below the MHD threshold. In the present case, the effective onset point is decreased only by less than 5%. How generic this finding is remains to be investigated, but the basic trend (a moderate linear reduction which is not extended by nonlinear effects) may be expected to hold.

Having discussed the existence and properties of regime transitions, we would now like to turn to an explanation of the qualitative form of the transport curves. The next section will be devoted to this topic.

V. β SCALING OF TRANSPORT LEVELS

There are some features in Fig. 8 that cannot be explained by the linear physics. Most prominently, the high-β end of the TEM-ITG regime has a saturation level that is lower than the electrostatic ITG level by a factor of about 20, which exceeds the respective decrease of the linear growth rate by an order of magnitude. Also, the knee in the electron magnetic transport at $\beta = 0.8\%$ – which to a lesser extent can also be found in the electron electrostatic transport – does not exist in any form in the linear simulations. These issues will be discussed in more detail now.

10

A. ITG-TEM transport levels

It is known that the nonlinear transport levels often tend to follow the linear growth rates. While here, such a model would correctly predict some general tendencies (declining ITG transport, constant TEM transport, KBM threshold), it can not explain the steep decline of the ion electrostatic transport at moderate β values. In the following, we seek to provide an explanation for this feature.

In a first step, we focus on the regime around $\beta \sim 1.2\%$, in which TEMs dominate linearly. TEM-induced transport has been estimated successfully before by means of a transport model which is described in detail in Refs. [27, 28]. While applying this model to turbulence simulations requires a nonlinear reference value, one can infer many interesting transport properties from linear simulations alone.

In Fig. 12, an ω_{Te} scan is presented which is based on this transport model. One can distinguish two regions, one with slowly and one with more strongly increasing transport. Clearly, the value used for the simulations shown in Fig. 8 is on the low transport region. While there is no absolute meaning to that transport value, it serves as an indication that one might indeed find a low saturation level at $\beta \sim 1.2\%$. In addition, a comparison between the qualitative behavior of the transport model and the growth rate at $k_y = 0.2$, $\gamma_{0.2}$, hints at an overestimation of the transport when making predictions from the linear behavior in Fig. 1: at $\omega_{\mathrm{Te}} = 6.89$, the ratio of the transport model value to $\gamma_{0.2}$ is especially low. Consequently, at this gradient, the nonlinear transport can be expected to drop to levels significantly lower than one might predict from the linear growth rate alone.

Another contributing factor could be the nonlinear interaction of the TEM turbulence with ITG modes, and possibly KBMs. Linear modes can compete nonlinearly and thus cancel each other out to a significant degree, reducing the transport levels (see, e.g., Ref. [16]). In Fig. 9, coexistence of phase relations at the regime transitions can be seen; and in Fig. 10, the regime signature transport peaks become blurred at β values close to the linear ITG-TEM transition. This coexistence implies interaction and competition, likely contributing to the reduction of the transport levels observed at moderate and high β. Yet another important effect is due to the presence of zonal flows which shall be discussed next.

B. Zonal flows and zonal fields

It is well known that in suppressing heat and particle transport, zonal flows can play a significant role (see Ref. [29] for a review on zonal flows). For the entire β range, an inspection of contour plots shows that zonal flows are strongly excited, becoming even more pronounced as β is increased. A quantitative measure of the impact of zonal flows is the shearing rate,

$$\omega_s = \frac{\mathrm{d}^2\Phi_{\mathrm{zon}}}{\mathrm{d}x^2} \ , \tag{2}$$

where Φ_{zon} is the zonal component of the electrostatic potential. Due to finite-frequency corrections [30], the shearing rate needs to be much larger than the linear growth rate, $\omega_s \gg \gamma$, for zonal flows to be able to act as the dominant nonlinear saturation mechanism, controlling the transport levels. As can be seen in Fig. 13, this necessary condition seems to be (marginally) fulfilled across the entire β range, with $\omega_s/\gamma \sim 10$. Moreover, for $\beta \leq 1.0\%$, ω_s/γ is steadily increasing. This finding suggests that zonal flows may contribute to the strong decrease of the transport level with increasing β.

In order to test this conjecture, we have repeated some simulations, removing the zonal component of the electrostatic potential and looking at the impact on the transport levels. Such modified simulations at $\beta = 0.1\%$ and $\beta = 0.6\%$ yielded no significant increase in the electrostatic heat flux (while effectively suppressing the electromagnetic contribution), indicating that for the lower-β range of the ITG-TEM regime, zonal flows contribute little to the drop in turbulent transport with increasing β. However, at $\beta = 1.25\%$, removing the zonal potential results in an increase especially of the ion but also the electron electrostatic transport levels by factors of ~ 3 and ~ 2 respectively. The electron electromagnetic level drops to very low levels, much like in the low β cases. This indicates that at higher β in the ITG-TEM regime, zonal flows become a major contributor in suppressing turbulent transport. In consequence, the low levels of high-β ITG-TEM transport can in part be explained by the effect of zonal flows.

Additionally, one can measure the effective shear due to magnetic field fluctuations (see, e.g., Ref. [31]). Following Ref. [32], we compute the magnetic shear fluctuation due to zonal fields,

$$\tilde{s} = q_0 \frac{R}{B_{\mathrm{ref}}} \frac{\mathrm{d}B_y}{\mathrm{d}x} \ . \tag{3}$$

The results can be found in Fig. 14. At its maximum at $\beta = 0.8\%$, $\tilde{s}/\hat{s} \approx 15\%$, making

$\tilde{s}$ a non-negligible quantity. Since the maximum coincides with a qualitative change in the nonlinear transport, it might follow that the nonlinear frequency shift at that value is in part due to the magnetic shear fluctuations. However, if this is to hold, the new frequency would still be purely nonlinear, for linear simulations with $\hat{s} = 0.786 \pm 0.15$ show only small modifications in their frequencies ($\omega = 0.627$ for $\hat{s} = 0.636$, and $\omega = 0.694$ for $\hat{s} = 0.936$) compared with $\hat{s} = 0.786$ ($\omega = 0.656$). Again, these results were obtained for $k_y = 0.2$. They indicate that in the present simulations, zonal fields are relatively strong, but still too weak to act as the dominant saturation mechanism.

C. Magnetic transport

One important question in the context of electromagnetic turbulence simulations which we have not yet discussed is the role of magnetic transport. By this expression, we refer to the contributions to the overall cross-field transport induced by (radial) magnetic field fluctuations. As is well known, the transport channel which is most affected by this process is the electron heat flux, Q_e. Its electromagnetic part Q_e^{em}, due to efficient parallel heat conduction along radially perturbed field lines, is plotted for the ITG regime – as a function of β – in Fig. 15. Surprisingly, the (quasi-)linear and nonlinear curves deviate substantially from one another. To good approximation, they scale like $Q_e^{em} \propto \beta$ and $Q_e^{em} \propto \beta^2$, respectively. The same applies to the transport values reported in Ref. [11].

In order to understand these simulation results, we make use of a simple model describing test particle transport along perturbed field lines. The latter has been used before in Ref. [8] and goes back to work by Rechester and Rosenbluth [33] in 1978. It is based on the ansatz

$$Q_e^{em} = \frac{\langle \tilde{q}_{e\parallel} \tilde{B}_x \rangle}{B_{ref}} \, , \tag{4}$$

$$\tilde{q}_{e\parallel} = -n_{e0}\chi_{e\parallel} \left(\frac{d\tilde{T}_{e\parallel}}{dz} + \frac{\tilde{B}_x}{B_{ref}} \frac{d\tilde{T}_{e\parallel}}{dx} + \frac{\tilde{B}_x}{B_{ref}} \frac{dT_{e0}}{dx} \right) \, . \tag{5}$$

Here, $\tilde{B}_x$ is the radial component of the magnetic field fluctuations, while $\tilde{T}_{e\parallel}$ corresponds to parallel electron temperature fluctuations. The three terms in the large brackets describe, collectively, the parallel temperature gradient along perturbed field lines. For the following discussion, they shall be labeled $\mathcal{T}_1$, $\mathcal{T}_2$, and $\mathcal{T}_3$, respectively.

As it turns out, one can interpret the findings shown in Fig. 15 by analyzing the GENE

data concerning phase relations between pairs of fluctuating quantities entering in the above model. For linear simulations, the nonlinear term $\mathcal{T}_2$ vanishes. At the same time, $\tilde{T}_{e\parallel}$ and $\tilde{q}_{e\parallel}$ have a phase relation of $\sim \pi/4$, whereas $\tilde{B}_x$ and $\tilde{q}_{e\parallel}$ are out of phase. Consequently, $\mathcal{T}_1 \gg \mathcal{T}_3$. Assuming that $\tilde{B}_x/B_{\mathrm{ref}} \propto \beta$, one thus obtains the prediction $Q_e^{\mathrm{em}}/Q_i^{\mathrm{es}} \propto \beta$ which is in line with the linear result shown in Fig. 15. Nonlinearly, however, one finds $Q_e^{\mathrm{em}}/Q_i^{\mathrm{es}} \propto \beta^2$ (see Fig. 15). This change can also be explained by the model. Due to random phases between $\tilde{T}_{e\parallel}$ and $\tilde{q}_{e\parallel}$, $\mathcal{T}_1$ is small. The same is true for $\mathcal{T}_2$, since $\tilde{B}_x$ and $\tilde{T}_{e\parallel}$ have a phase of ~ 0. Moreover, $\tilde{B}_x$ and $\tilde{q}_{e\parallel}$ have a phase of $\sim -\pi/4$, resulting in $\mathcal{T}_3 \propto \beta^2$ becoming the dominant term. Consequently, for the magnetic component of the (nonlinear) electron thermal diffusivity, the equation

$$\chi_e^{\mathrm{em}} = \chi_{e\parallel} \langle (\tilde{B}_x/B_{\mathrm{ref}})^2 \rangle \tag{6}$$

can be used. This leaves one to determine the parallel diffusivity, $\chi_{e\parallel}$. For a sheared slab magnetic field geometry, this quantity was calculated (see Ref. [34]) to be

$$\chi_{e\parallel} \approx \frac{1}{k_\parallel} \left(\frac{T_e}{m_e} \right)^{1/2} \sim q_0 R \left(\frac{T_e}{m_e} \right)^{1/2} \tag{7}$$

in the adiabatic limit. While technically, there is no quantity $k_\parallel$ for radially extended modes in a sheared magnetic field (due to the quasi-periodic boundary conditions), one can still use this expression as an approximation.

In Fig. 16, the predictions due to these equations are compared with the simulation results. Very good agreement between the model and the real magnetic transport is obtained when multiplying $\chi_{e\parallel}$ by a scalar quantity η of order unity. η depends on the shape of the extended ballooning mode structure and will therefore not necessarily be identical for different turbulence regimes. In fact, we found that $\eta_{\mathrm{ITG}} = 0.625 \pm 0.026$ in the range from $\beta = 0.3\%$ to $\beta = 1.0\%$ (as expected, the model breaks down as $\beta \to 0$). For the high-β end of the ITG-TEM regime as well as the KBM regime, there is little statistics; the corresponding values are $\eta_{\mathrm{ITG-TEM}} = 0.37$ and $\eta_{\mathrm{KBM}} = 0.46$. Note that all these values are rather similar, and that within a single regime, there is no significant β dependence of η. Also note that this transport model seems to distinguish nonlinear regimes along the lines of the linear regimes, not changing η at $\beta = 0.8\%$.

VI.   CONCLUSIONS

In the present paper, we have shown results of both linear and nonlinear gyrokinetic simulations with the GENE code for Cyclone Base Case parameters and β values ranging from zero up to above the KBM threshold. The β scaling of the turbulent transport is found to be linked to a rather complex interplay of linear and nonlinear effects. While the rough trend (stabilization with increasing β up to the KBM onset) could be expected on the basis of linear growth rates, the strength of this effect (decrease by a factor of about 20) could not. Likely, the latter is mainly due to a combination of zonal flow effects and destructive interference between co-existing modes. The change of the dominating linear mode from ITG to TEM at moderate β values was reflected in the simulation results, but no pure TEM regime was found.

Using GENE as an eigenvalue solver and varying the nominal temperature and density gradients, we found that the reduction of the linear KBM threshold relative to its MHD counterpart tends to remain below about 20%. Moreover, the disappearance of the KBM can occur in (at least) three different ways: it can turn into a damped mode; it can become marginally stable; or it can transition directly into a different mode (like a TEM or an ITG mode). Nonlinearly, however, the β value for which the turbulence acquires a clear KBM character is very close to the point at which the KBM growth rate exceeds that of a TEM. This finding suggests that KBMs are only likely to dominate nonlinearly wherever they dominate linearly. In the present case, the effective KBM onset point is decreased with respect to the MHD threshold by less than 5%.

The role of magnetic electron heat transport (due to efficient parallel heat conduction along radially perturbed field lines) has also been studied. Here, the nonlinear simulations yield $Q_{\mathrm{e}}^{\mathrm{em}} \propto \beta^2$ which cannot be explained (quasi-)linearly. However, employing a test particle transport model in the spirit of Rechester and Rosenbluth, and analyzing the GENE data with respect to phase relations between pairs of fluctuating quantities entering in this model, one finds very good agreement with the simulation results. Here, a scalar prefactor had to be introduced, but it turned out to always be around unity and practically independent of β within any single regime.

In terms of comparing simulation results with experimental measurements, it is interesting to note the following feature. Electrostatic (two-species) gyrokinetic simulations of core

turbulence using Cyclone Base Case parameters are known to yield transport levels which are almost two orders of magnitude higher than the respective experimental values. However, taking into account finite-β effects and employing the realistic value of $\beta_{\mathrm{CBC}} \sim 1.0\%$, the (dominant) electrostatic ion heat flux decreases by a factor of 5-10. Consequently, electromagnetic effects may account for a significant share of the discrepancy between the simulations and the experiment. Additionally, other effects may contribute to closing the gap, most prominently edge transport (for electromagnetic edge turbulence investigations by means of a fluid model, see Ref. [35]); another factor would be switching from the $\hat{s}$-α model to a more realistic magnetic geometry. First investigations have been reported in Ref. [36], but further research will be required to understand the role of realistic geometry for electromagnetic simulations in more detail.

[1] D.C. McDonald, J.G. Cordey, C.C. Petty, M. Beurskens, R. Budny, I. Coffey, M. de Baar, C. Giroud, E. Joffrin, P. Lomas, A. Meigs, J. Ongena, G. Saibene, R. Sartori, I. Voitsekhovitch, and JET EFDA contributors, Plasma Phys. Control. Fusion **46**, A215 (2004)

[2] C.C. Petty, T.C. Luce, D.C. McDonald, J. Mandrekas, M.R. Wade, J. Candy, J.G. Cordey, V. Drozdov, T.E. Evans, J.R. Ferron, R.J. Groebner, A.W. Hyatt, G.L. Jackson, R.J. La Haye, T.H. Osborne, and R.E. Waltz, Phys. Plasmas **11**, 2514 (2004)

[3] L. Vermare, F. Ryter, C. Angioni, A.G. Peeters, J. Stober, R. Bilato, L.D. Horton, B. Kurzan, C.F. Maggi, H. Meister, J. Schirmer, G. Tardini, and the ASDEX Upgrade Team, Nucl. Fusion **47**, 490 (2007)

[4] D.C. McDonald, L. Laborde, J.C. DeBoo, F. Ryter, C.D. Challis, P. de Vries, J. Hobirk, E. Joffrin, T.C. Luce, J. Mailloux, V. Pericoli-Ridolfini, A.C.C. Sips, K. Thomsen, and JET EFDA contributors, 35th EPS Conference on Plasma Physics, Hersonissos (2008)

[5] P.B. Snyder and G.W. Hammett, Phys. Plasmas **8**, 744 (2001)

[6] B.D. Scott, Plasma Phys. Control. Fusion **45**, A385 (2003)

[7] B.D. Scott, Plasma Phys. Control. Fusion **48**, B277 (2006)

[8] F. Jenko and W. Dorland, Plasma Phys. Control. Fusion **43**, A141 (2001)

[9] Y. Chen, S.E. Parker, B.I. Cohen, A.M. Dimits, W.M. Nevins, D. Shumaker, V.K. Decyk, and J.N. Leboeuf, Nucl. Fusion **43**, 1121 (2003)

[10] S.E. Parker, Y. Chen, W. Wan, B.I. Cohen, and W.M. Nevins, Phys. Plasmas **11**, 2594 (2004)

[11] J. Candy, Phys. Plasmas **12**, 72307 (2005)

[12] F. Jenko, W. Dorland, M. Kotschenreuther, and B.N. Rogers, Phys. Plasmas **7**, 1904 (2000)

[13] T. Dannert and F. Jenko, Phys. Plasmas **12**, 72309 (2005)

[14] A.M. Dimits, G. Bateman, M.A. Beer, B.I. Cohen, W. Dorland, G.W. Hammett, C. Kim, J.E. Kinsey, M. Kotschenreuther, A.H. Kritz, L.L. Lao, J. Mandrekas, W.M. Nevins, S.E. Parker, A.J. Redd, D.E. Shumaker, R. Sydora, and J. Weiland, Phys. Plasmas **7**, 969 (2000)

[15] A.J. Brizard and T.S. Hahm, Rev. Mod. Phys. **79**, 421 (2007)

[16] F. Merz, Ph.D. thesis, University of Münster (2008)

[17] P. Xanthopoulos and F. Jenko, Phys. Plasmas **13**, 092301 (2006)

[18] M. Kammerer, F. Merz, and F. Jenko, Phys. Plasmas **15**, 52102 (2008)

[19] M. Kotschenreuther, G. Rewoldt, and W.M. Tang, Comput. Phys. Commun. **88**, 128 (1995)

[20] P.B. Snyder, Ph.D. thesis, Princeton University (1999)

[21] M.S. Chu, C. Chu, G. Guest, J.Y. Hsu, and T. Ohkawa, Phys. Rev. Lett. **41**, 247 (1978)

[22] C.Z. Cheng, Phys. Fluids **25**, 1020 (1982)

[23] F. Zonca, L. Chen, J.Q. Dong, and R.A. Santoro, Phys. Plasmas **6**, 1917 (1999)

[24] J. Dong, L. Chen, and F. Zonca, Nucl. Fusion **39**, 1041 (1999)

[25] G.L. Falchetto, J. Vaclavik, and L. Villard, Phys. Plasmas **10**, 1424 (2003)

[26] G. Zhao and L. Chen, Phys. Plasmas **9**, 861 (2002)

[27] F. Jenko, T. Dannert, and C. Angioni, Plasma Phys. Control. Fusion **47**, B195 (2005)

[28] M. Kotschenreuther, W. Dorland, M.A. Beer, and G.W. Hammett, Phys. Plasmas 2, 2381 (1995)

[29] P.H. Diamond, S.-I. Itoh, K. Itoh, and T.S. Hahm, Plasma Phys. Control. Fusion **47**, R35 (2005)

[30] T.S. Hahm, M.A. Beer, Z. Lin, G.W. Hammett, W.W. Lee, and W.M. Tang, Phys. Plasmas **6**, 922 (1999)

[31] C. Holland and P.H. Diamond, Phys. Plasmas **9**, 3857 (2002)

[32] F. Jenko and A. Kendl, Phys. Plasmas **9**, 4103 (2002)

[33] A.B. Rechester and M.N. Rosenbluth, Phys. Rev. Lett. **40**, 38 (1978)

[34] Z. Chang and J.D. Callen, Phys. Fluids B **4**, 1167 (1992)

[35] B. Scott, Plasma Phys. Control. Fusion **39**, 1635 (1997)

[36] M.J. Pueschel, L. Laborde, and F. Jenko, 35th EPS Conference on Plasma Physics, Hersonissos (2008)
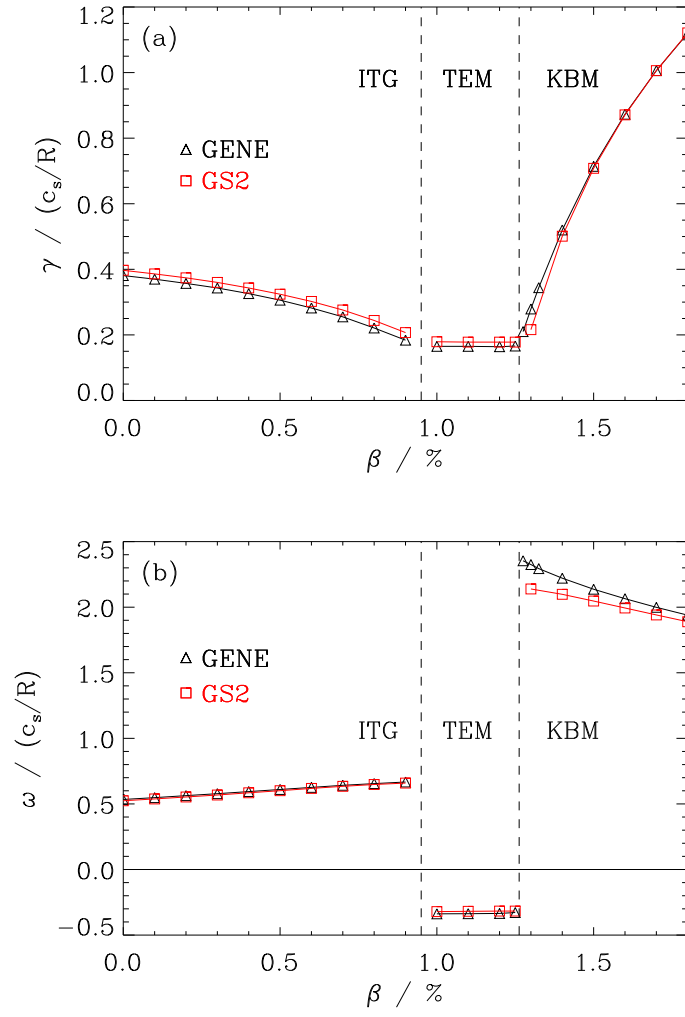
FIG. 1: (Color online) Dependence of growth rate γ (a) and real frequency ω (b) on the plasma β for $k_y = 0.2$. GENE results are shown as black triangles, GS2 results as red squares. There is very good agreement between the two codes. Clearly, three instability regimes can be discerned: ITG, TEM, and KBM.
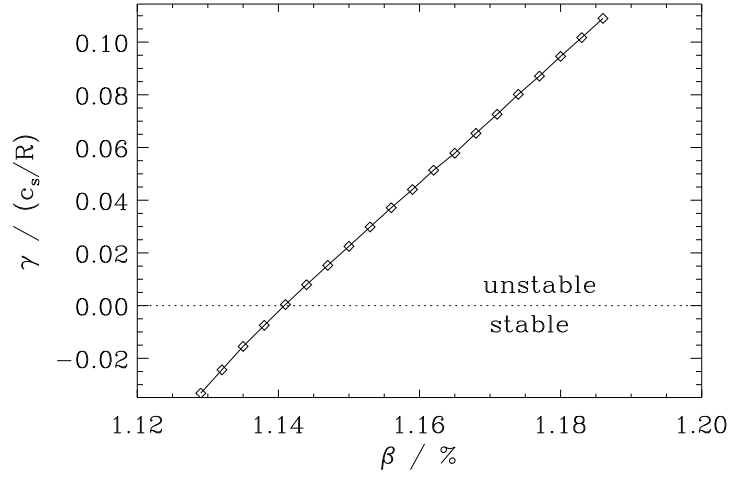
FIG. 2: Subdominant growth rates of the kinetic ballooning mode (KBM). At $\beta = 1.14\%$, the mode becomes linearly unstable. No marginal stability is observed below this value.
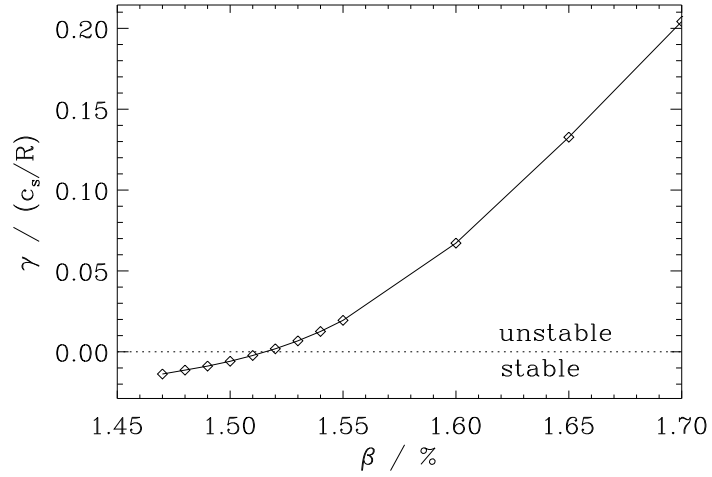
FIG. 3: Subdominant growth rates of the kinetic ballooning mode (KBM) for a set of physical parameters differing from the standard set used in this work (as given in the text). Here, one observes a knee below the zero line. For smaller β values, the mode remains marginally stable.
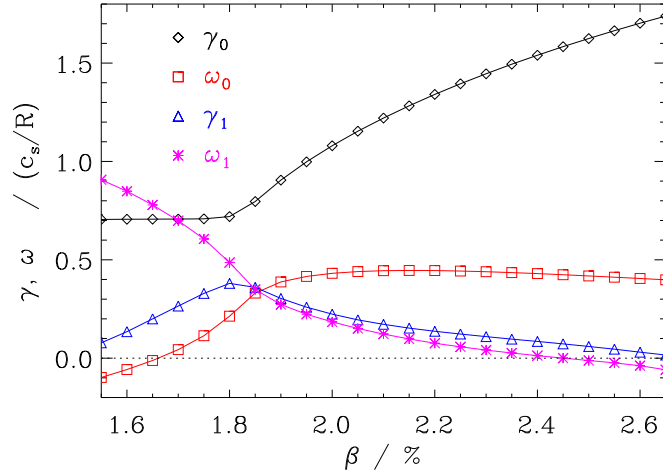
FIG. 4: (Color online) Transformation of a KBM into a TEM-like mode. As β is decreased, the KBM frequency ω_0 (red squares) continuously drops to negative levels. Correspondingly, the growth rate γ_0 (black diamonds) stops its descent and becomes constant. This behavior can be understood by looking at another mode, characterized by γ_1 (blue triangles) and ω_1 (pink stars): originally (i.e., for a smaller density gradient ω_n), the left branch of γ_0 was connected to the right branch of γ_1, and conversely, the KBM-like right branch of γ_0 used to be connected to the left branch of γ_1. The same goes for the frequencies.
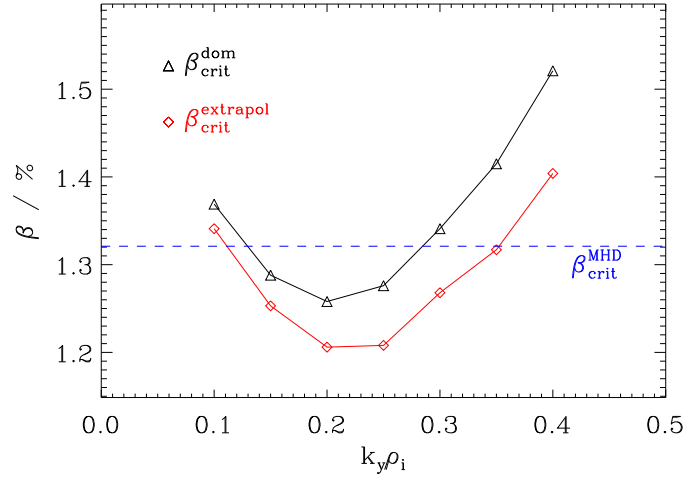
FIG. 5: (Color online) Critical values of β for the onset of KBMs and their dominance over TEMs, respectively, for a range of toroidal mode numbers. Black triangles mark the values where the KBMs become dominant, whereas the extrapolated critical β for subdominant instability of the KBMs is marked by red diamonds. For comparison, the MHD prediction is shown as a blue dashed line.
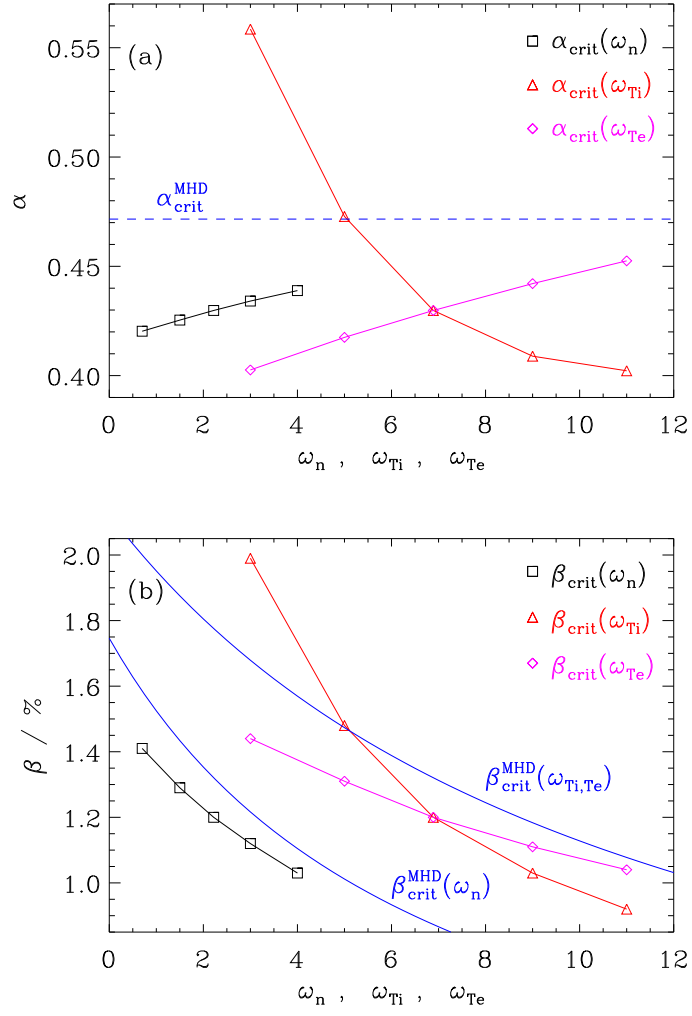
FIG. 6: (Color online) Dependence of critical β (a) and α (b) values for the onset of KBMs on the gradients on the density gradient (black squares), the ion temperature gradient (red triangles), and the electron temperature gradient (pink diamonds). For comparison, the MHD predictions are shown in blue. For this data, $k_y = 0.2$.
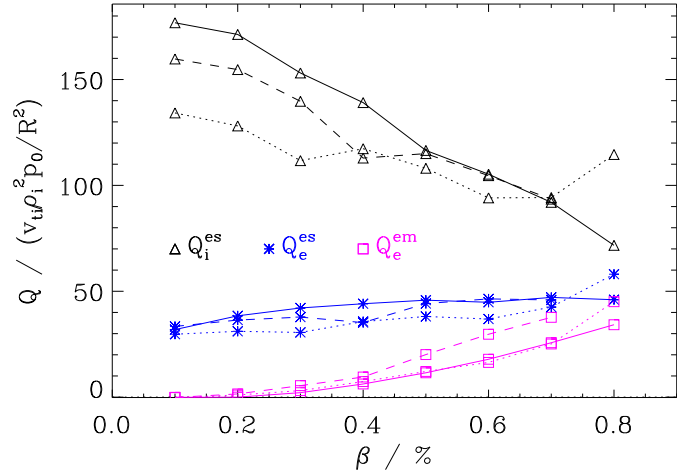
FIG. 7: (Color online) Comparison of GENE and GYRO (as reported in Ref. [11]; dotted lines) transport levels (black triangles for the ion electrostatic heat flux, blue stars for the electron electrostatic heat flux, and pink squares for the electron electromagnetic heat flux). For GENE, both the reference values (solid lines) and additional simulation results (with lower resolution, more comparable to that in Ref. [11]; dashed lines) are shown.
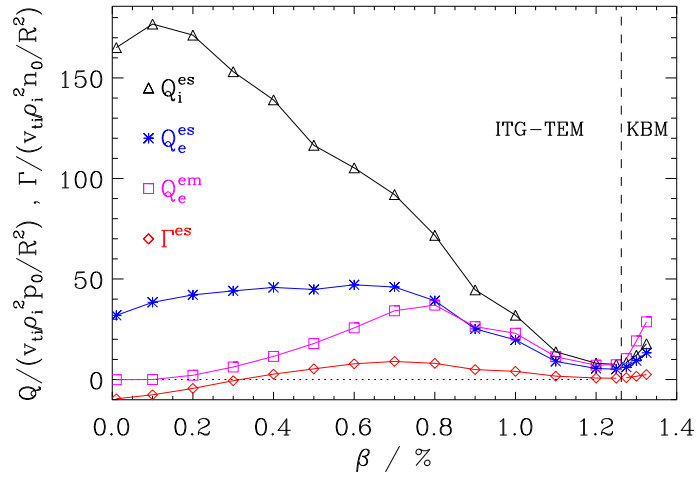
FIG. 8: (Color online) Heat and particle transport as a function of β. The values for the ion electromagnetic heat flux and the electromagnetic particle flux are very small and therefore were not included in this figure. The ion electrostatic heat flux reflects the behavior of the linear growth rates. However, while a KBM dominant regime can be distinguished, a pure TEM regime is not found.
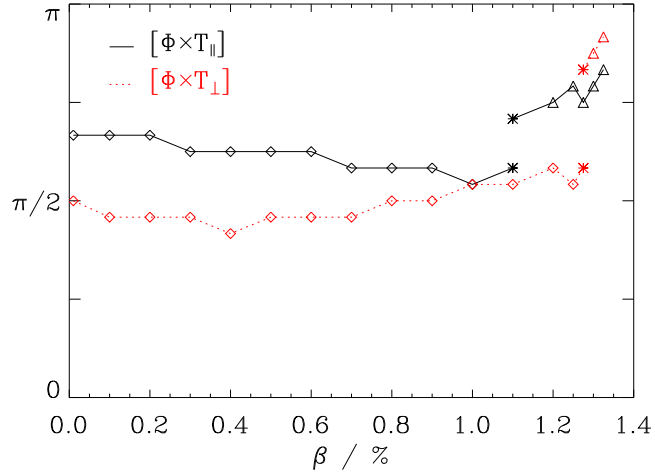
FIG. 9: (Color online) Cross phase changes with increasing β. Solid black lines represent the dominant phases between the electrostatic potential and the parallel ion temperature, whereas dotted red lines represent the dominant phases between the electrostatic potential and the perpendicular ion temperature. Within every regime, phases change only very little and continuously (diamonds and triangles), but at two of the characteristic β values, a phase splitting occurs (stars).
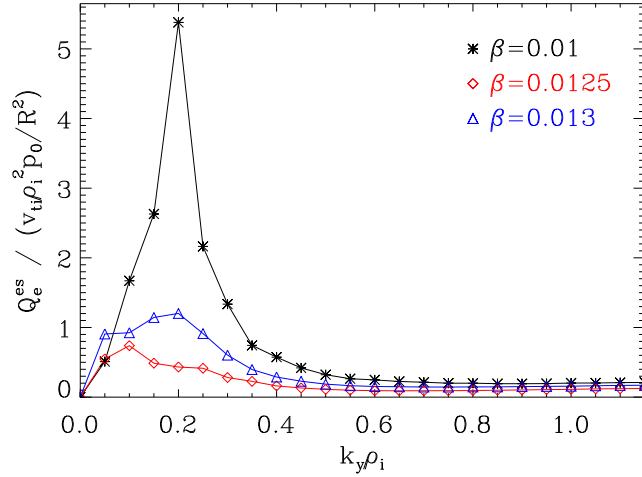

FIG. 10: (Color online) Changes in the electrostatic electron transport spectra with increasing β; the ion counterpart shows a very similar behavior. At $\beta = 1.25\%$, the peak shifts slightly to lower k_y while retaining strong transport contributions at $k_y = 0.2$.
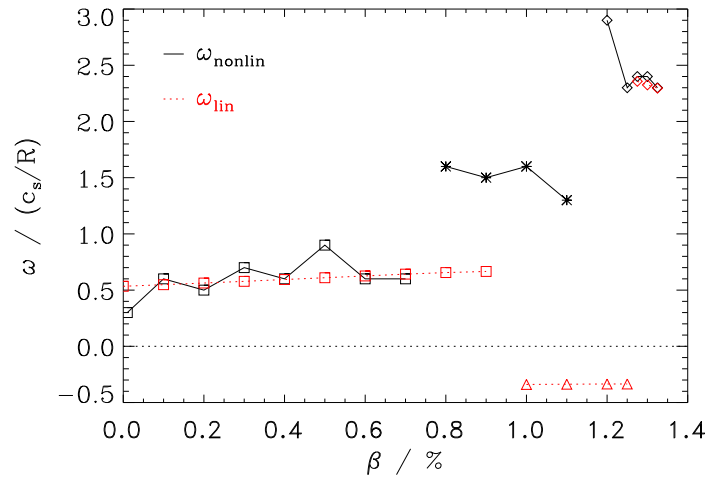
FIG. 11: (Color online) Nonlinear frequencies at $k_y = 0.2$ (solid black curves), extracted via Fourier transform of the electrostatic potential, Φ. The linear frequencies are included for comparison (dotted red curves). Note that the KBM frequencies take over before the transport is dominated by these modes. Nonlinearly, there is a frequency regime between the ITG and the KBM level (stars) which exists roughly but not exactly at β values that correspond to the TEMs linearly (triangles).
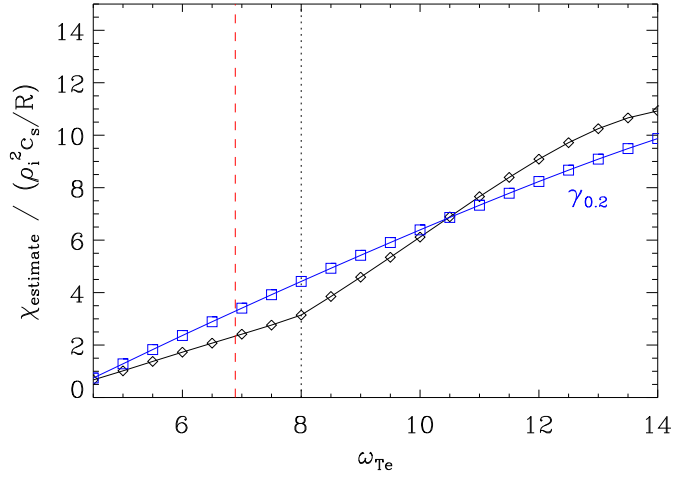
FIG. 12: (Color online) Linear TEM transport model. Shown is the predicted scaling of the thermal diffusivity $\chi_{\text{estimate}} = (\gamma/\langle k_\perp^2 \rangle)_{\text{max}}$ with the electron temperature gradient. At $\omega_{\text{Te}} = 8.0$ (black dotted line), one observes a knee where the scaling changes. The value $\omega_{\text{Te}} = 6.89$ (red dashed line) used in the nonlinear simulations lies on the low transport branch. $\gamma_{0.2}$ is the linear growth rate at $k_y = 0.2$ rescaled to arbitrary units.
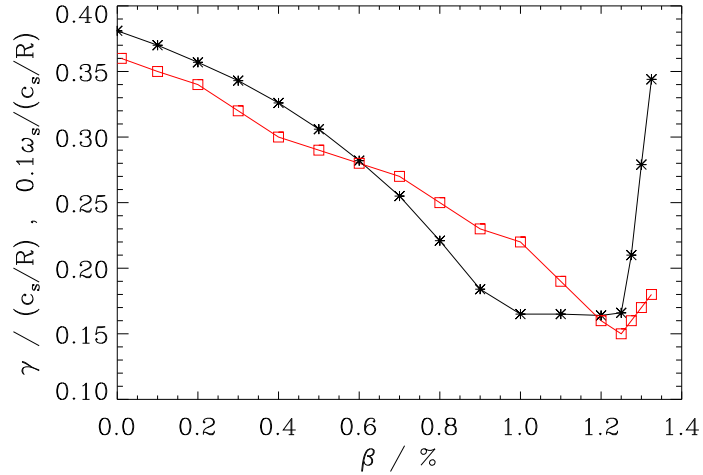
FIG. 13: (Color online) Comparison of the shearing rate ω_s (red squares; rescaled) and the linear growth rate γ (black stars). The requirement for zonal flow based transport suppression, $\omega_s \gg \gamma$, is fulfilled at every point in the ITG-TEM regime.
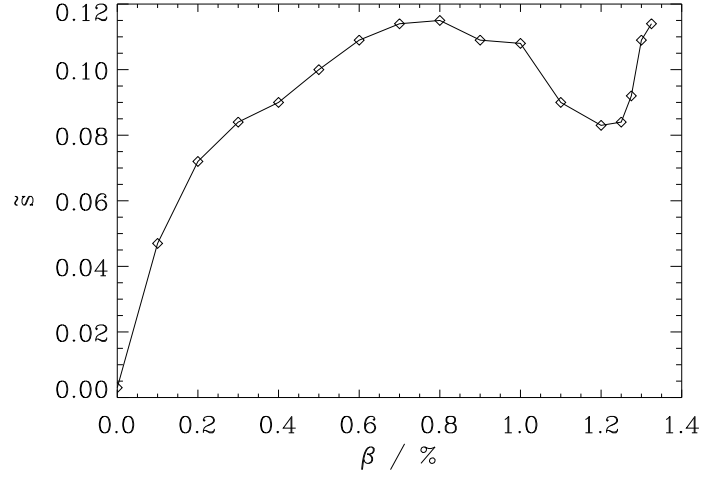
27

FIG. 14: Magnetic shear fluctuations as a function of β. Note that while $\tilde{s}$ always remains smaller than the global shear, $\hat{s} = 0.786$, it still makes for a significant modification.
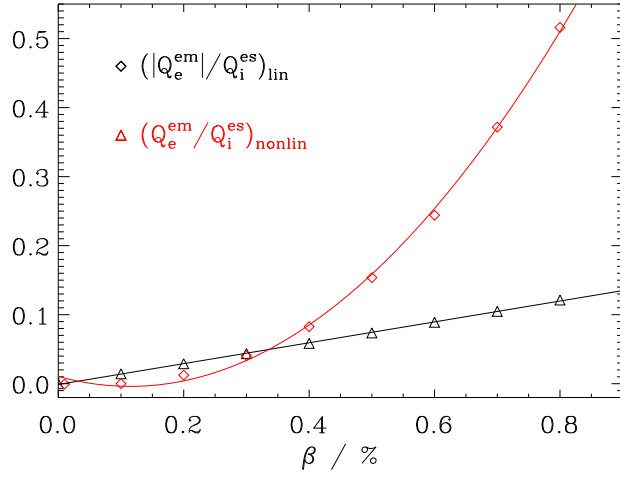

FIG. 15: (Color online) Linear and nonlinear scaling of the electron magnetic transport with β: the linear values (black triangles) can be fitted excellently by a straight line, the nonlinear values (red diamonds) by a quadratic function, as shown here.
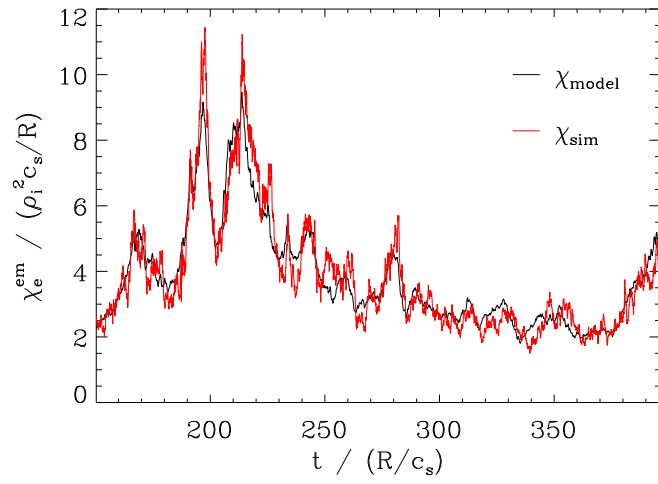
FIG. 16: (Color online) Electron magnetic transport as seen in the simulation (red curve) and as predicted by a simple model (black curve). One free scalar prefactor was found to be of order unity.